

Strain-dependent exciton diffusion in transition metal dichalcogenides

Roberto Rosati,^{1,*} Samuel Brem,¹ Raül Perea-Causín,¹ Robert Schmidt,² Iris Niehues,² Steffen Michaelis de Vasconcellos,² Rudolf Bratschitsch,² and Ermin Malic¹

¹*Chalmers University of Technology, Department of Physics, 412 96 Gothenburg, Sweden*

²*Institute of Physics and Center for Nanotechnology, University of Münster, 48149 Münster, Germany*

Monolayers of transition metal dichalcogenides (TMDs) have a remarkable excitonic landscape with deeply bound bright and dark exciton states. Their properties are strongly affected by lattice distortions that can be created in a controlled way via strain. Here, we perform a joint theory-experiment study investigating exciton diffusion in strained tungsten disulfide (WS_2) monolayers. We reveal a non-trivial and non-monotonic influence of strain. Lattice deformations give rise to different energy shifts for bright and dark excitons changing the excitonic landscape, the efficiency of intervalley scattering channels, and the weight of single exciton species to the overall exciton diffusion. We predict a minimal diffusion coefficient in unstrained WS_2 followed by a steep speed-up by a factor of 3 for tensile biaxial strain at about 0.6% strain - in excellent agreement with our experiments. The obtained microscopic insights on the impact of strain on exciton diffusion are applicable to a broad class of multi-valley 2D materials.

Transition metal dichalcogenides (TMDs) and related van der Waals heterostructures have attracted much attention in current research due to their remarkable excitonic landscape including bright, spin- and momentum-dark, and spatially separated exciton states [1–8]. Optical properties of TMDs are strongly sensitive to lattice distortions, as shown for spatially-homogenous [9–16] and spatially-inhomogeneous strain [17–24]. Strain-induced lattice deformations [see Fig. 1a] induce changes in the energy and in the effective mass of electronic valleys [11, 25–28] resulting in a qualitative change of the excitonic landscape and efficiency of exciton-phonon scattering channels (Fig. 1b) [14, 27, 28].

Strain is expected to have an important impact also on transport in TMDs, e.g. spatially inhomogeneous strain acts as a driving force for exciton/carrier funneling [22, 24, 29], similarly to bias fields for charged particles [30, 31] or gauge potentials for interlayer excitons in van der Waals heterostructures [32]. Even in the absence of additional driving forces, an initial spatially-localized excitonic occupation spreads in space due to the occupation gradient resulting eventually in a conventional exciton diffusion [33], as sketched in Fig. 1c. While in the presence of one single valley the diffusion is expected to be only quantitatively altered by strain through e.g. changes in the effective masses, the multi-valley exciton landscape in TMDs promises interesting strain effects. The diffusion is expected to be dominated by the most populated, energeti-

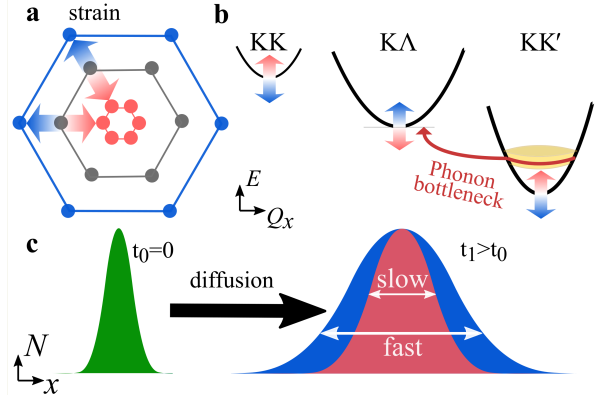


FIG. 1. Strain-dependent exciton diffusion. Biaxial strain implies (a) lattice deformations, which modify (b) the excitonic landscape by different spectral shifts of the bright KK and momentum-dark KA and KK' excitons. This can introduce strain-dependent phonon bottlenecks for intervalley scattering. (c) As a result, an initial spatially-localized exciton occupation diffuses slower or faster depending on the applied strain.

cally lowest exciton valley [33–35], which might vary as a function of strain due to the strongly valley-dependent energy shifts [Fig. 1b]. Since different valleys have different valley-intrinsic diffusion coefficients [33], this leads to strain-induced changes of the overall diffusion, see Fig. 1c. Furthermore, strain-induced energy shifts also change the possibility for phonon-induced intervalley scattering channels and may even result in phonon bottlenecks at specific strain values [Fig. 1b]. This has also a direct impact on the efficiency of exciton diffusion.

Based on a fully quantum-mechanical approach and supported by experimental measurements, our

* roberto.rosati@chalmers.se

work provides microscopic insights into the interplay of exciton diffusion and strain in the WS₂ monolayer as an exemplary TMD material. We microscopically address the evolution of optically excited, spatially localized excitons resolved in time, momentum, and space. We take into account bright and momentum-dark excitonic states obtained by solving the Wannier equation under strain [27, 28]. We predict non-trivial dependence of the diffusion on strain, showing a non-monotonic behaviour, where the overall diffusion is either dominated by specific dark excitons or determined by intervalley scattering. This leads to a steep speed-up of the diffusion upon small tensile strain values - in excellent agreement with our spatiotemporal photoluminescence experiments.

I. RESULTS

Theoretical approach: Starting with the unstrained single-particle dispersion [36], we implement the strain-induced variations of effective masses and band extrema E_v [27]. For each strain value we then solve the Wannier equation [37–40] with a non-local Coulomb screening [41] to obtain a set of excitonic states $|\alpha\rangle \equiv |\mathbf{Q}, v\rangle$ labelled by the excitonic valley v and the center-of-mass momentum \mathbf{Q} . These states have the energy $\varepsilon_\alpha = E_v + \hbar^2|\mathbf{Q}|^2/(2M_v)$, which depends on strain largely via changes in E_v [27] [see also Fig. 1b], but also via changes in the total mass M_v . Due to considerable energetic separations to higher excitonic states, we restrict our investigations to the ground $1s$ exciton, however taking into account all relevant electronic valleys and the resulting bright KK as well as momentum-dark KK', K Λ , K Λ' , Γ K and Γ K' excitons [3]. Here, the first and the second letter denote the location of the Coulomb-bound hole and electron, respectively.

Now, we introduce the excitonic intravalley Wigner function $N_{\mathbf{Q}}^v(\mathbf{r}, t)$, which summed over \mathbf{Q} provides the intravalley spatial density $N_v(\mathbf{r}, t) \equiv \frac{1}{V} \sum_{\mathbf{Q}} N_{\mathbf{Q}}^v(\mathbf{r}, t)$ [33]. At the spatial and temporal scales considered here, $N_{\mathbf{Q}}^v(\mathbf{r}, t)$ can be directly interpreted as probability of finding excitons with momentum \mathbf{Q} in position \mathbf{r} and valley v . An equation of motion for the spatiotemporal dynamics of excitons can be introduced by exploiting the Heisenberg equation [33]. The derived equation can then be transformed into Wigner representation [42, 43] and

reads in the low excitation regime

$$\begin{aligned} \dot{N}_{\mathbf{Q}}^v(\mathbf{r}, t) = & \left(\frac{\hbar\mathbf{Q}}{M_v} \cdot \nabla - \gamma\delta_{\mathbf{Q},0}\delta_{v,KK} \right) N_{\mathbf{Q}}^v(\mathbf{r}, t) \\ & + \Gamma_{\mathbf{Q};0}^{v:KK} |p_0(\mathbf{r}, t)|^2 + \dot{N}_{\mathbf{Q}}^v(\mathbf{r}, t) \Big|_{sc}. \end{aligned} \quad (1)$$

The first term indicates the free evolution of excitons, while the second term takes into account the losses due to the radiative recombination γ within the light cone ($\delta_{\mathbf{Q},0}\delta_{v,KK}$) [38–40, 44].

The first contribution in the second line of Eq. (1) describes the formation of incoherent excitons due to phonon-driven transfer from the excitonic polarization $p_{\mathbf{Q}\approx 0}(\mathbf{r}, t)$. The process is driven by exciton-phonon scattering rates $\Gamma_{\mathbf{Q}v'}^{vv'}$, describing scattering from the state $|\mathbf{Q}'v'\rangle$ to $|\mathbf{Q}v\rangle$ via interaction with phonons [39, 40]. The last term in Eq. (1) describes the scattering contribution $\dot{N}_{\mathbf{Q}}^v(\mathbf{r}, t) \Big|_{sc} = \Gamma_{\mathbf{Q}}^{\text{in},v}(\mathbf{r}, t) - \Gamma_{\mathbf{Q}}^{\text{out},v} N_{\mathbf{Q}}(\mathbf{r}, t)$, which is dominated by exciton-phonon scattering in the considered low-excitation regime. It gives rise to a redistribution of the Wigner function in momentum toward a local equilibrium distribution, cf. the supplementary material for more details. Importantly, exciton-phonon scattering depends crucially on strain, mostly via the energies of the involved initial and final exciton states, while the variations of phonon energies or electron-phonon scattering are typically less relevant and are thus not considered here [27, 45]. In particular, strain-induced energy shifts can lead to drastic changes in intervalley scattering via opening or closing of scattering channels [see phonon bottleneck in Fig. 1b]. In contrast, intravalley scattering is only slightly influenced by strain via changes in the effective mass M_v [27, 46, 47].

In the steady-state regime the interplay between scattering-free propagation and scattering mechanisms implies that the spatial distribution evolves at first approximation according to the Fick's law $\dot{N}_v(\mathbf{r}, t) = D_v \Delta_{\mathbf{r}} N_v(\mathbf{r}, t)$, where decaying mechanisms have been omitted [48, 49]. Here, $D_v = 1/2 \langle \tau_{\mathbf{Q}}^v \hbar^2 Q^2 / M_v^2 \rangle_{\mathbf{Q}}^v$ is the diffusion coefficient with $1/\tau_{\mathbf{Q}}^v = \sum_{\mathbf{Q}',v'} \Gamma_{\mathbf{Q}'\mathbf{Q}}^{v'v}$ denoting the momentum-dependent relaxation times. We have introduced the expectation value $\langle f_{\mathbf{Q}} \rangle_{\mathbf{Q}}^v = \sum_{\mathbf{Q}} f_{\mathbf{Q}} \text{Exp}(-\frac{\varepsilon_{\mathbf{Q}v}}{k_B T}) / \sum_{\mathbf{Q}} \text{Exp}(-\frac{\varepsilon_{\mathbf{Q}v}}{k_B T})$. Under the assumption of constant relaxation times $\tau_{\mathbf{Q}}^v \approx \tau_v$ the well-known steady-state relation $D_v = \tau_v k_B T / M_v$ can be recovered. The overall diffusion of the total excitonic spatial density $N = \sum_v N_v$ can be affected by strain in two major ways: (i) Strain changes the relative occupation weight N_v/N of each valley. The overall

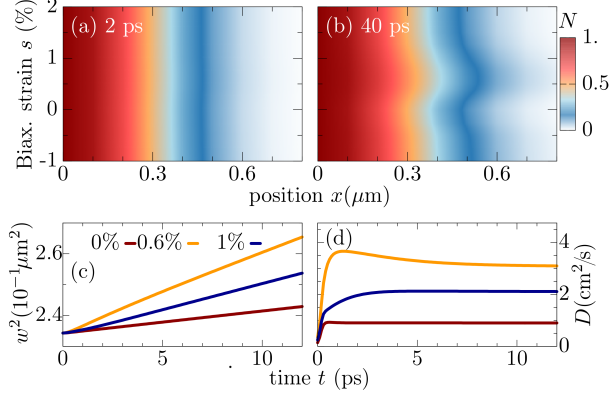


FIG. 2. **Spatiotemporal evolution under strain.** Strain-dependent spatial evolution of the exciton density N in a WS_2 monolayer on SiO_2 after a pulsed spatially-localized optical excitation. The spatial evolution is shown along the x axis at the fixed time of (a) 2 ps soon after the optical excitation and after (b) 40 ps. For given strain values, we show the evolution of the corresponding (c) squared spatial width w^2 and the (d) associated effective diffusion coefficient D .

diffusion will be dominated by the most populated valley and its own valley-intrinsic diffusion [33]. (ii) Strain changes the efficiency of the scattering channels through shifting the energies of initial and final scattering states, which crucially determine the velocity of exciton diffusion.

Strain-dependent exciton diffusion: Exploiting Eq. (1), we have a microscopic access to the spatially and temporally resolved dynamics of excitons in strained TMDs. In the main manuscript, we focus on the exemplary case of WS_2 monolayers on a SiO_2 substrate. In supplementary material, we also discuss the exciton diffusion in strained WSe_2 , MoSe_2 , and MoS_2 monolayers. Figures 2(a)-(b) illustrate the strain dependent spatial evolution of the exciton density $N(\mathbf{r}, t)$ soon after the optical excitation [$t=2$ ps in (a)] and at a later time [$t=40$ ps in (b)]. We consider a pulsed optical excitation around $t = 0$ resonant to the bright exciton X_0 , and with a Gaussian spatial confinement corresponding to a full-widths-half-maximum of 800 nm in amplitude and a temporal duration of 200 fs. This generates an initial strain-independent excitonic distribution, cf. Fig. 2a. After few tens of picoseconds, the spatial distribution becomes broader and the width is strongly strain dependent, cf. Figs. 2(b). We find in particular a faster spatial spreading for given strain values s , e.g. $s \approx 0.6\%$. The differences in exciton diffusion are not monotonic in strain: Increasing the strain from negative (compressive) to positive (ten-

sile) values, the diffusion initially becomes slower from -1% to 0% strain, then it speeds up steeply as the strain increases to 0.6% and finally it slows down again for larger strain values.

The spatial broadening of the exciton density N can be quantified introducing a width w whose squared modulus is proportional to the variance $w^2 = \int \mathbf{r}^2 N(\mathbf{r}, t) d\mathbf{r} / N$. According to Fick's law, confined spatial distributions behave as $N(\mathbf{r}, t) \propto \exp[-r^2/w^2(t)]$ with $w^2(t) = w_0^2 + 4Dt$ [50, 51], where w_0 is the initial width. It follows that also in the microscopic case when evaluating Eq. (1) one can define an *effective diffusion coefficient* (also called *diffusivity*) $D = \frac{1}{4} \partial_t w^2$, i.e. as slope of the temporal evolution of the squared width w^2 . In Figs. 2(c) and (d) we plot the temporal evolution of squared width w^2 and the associated effective diffusion coefficient for three different values of strain. The squared width w^2 shows quickly a linear evolution for all strain values, although the slope varies crucially with strain indicating a strong strain-dependence of the exciton diffusion. We find that after an initial steep increase, the diffusion coefficient $D(t)$ reaches a stationary value after a few ps. This corresponds to the transition from a ballistic regime, i.e. scattering-free evolution with a quadratic w^2 and linear D , to the conventional diffusive regime with a linear w^2 and stationary $D(t) \equiv D$ [33]. Both strain-induced quicker ballistic-to-diffusive transition and smaller D values are signatures of more efficient scattering channels, as seen e.g. at 0% strain. Due to the very short ballistic-to-diffusive transition, it is the stationary diffusion coefficient D that determines the exciton diffusion in Fig. 2b.

Now, we investigate the strain-dependence of the stationary diffusion coefficient covering a larger range of compressive to tensile biaxial strain values, cf. Fig. 3a. We find saturation values for the diffusion coefficient of 2.2 and $0.4 \text{ cm}^2/\text{s}$ for compressive strain around -1% and tensile strain above $+1.6\%$, respectively. Furthermore, we predict a strongly non-monotonic strain-dependence including a relative minimum in the unstrained material (0% strain) and a maximum at about 0.6% tensile strain. This can be understood by decomposing the valley-dependent contribution to the overall exciton diffusion. Thin lines in Fig. 3a show the diffusion coefficient obtained considering a reduced excitonic valley landscape. In all cases we have taken into account the optically excited KK excitons together with only KK' (purple line) or KA and KA' (i.e. $\text{KA}^{(\prime)}$, orange line) or $\text{TK}^{(\prime)}$ (green line) excitons,

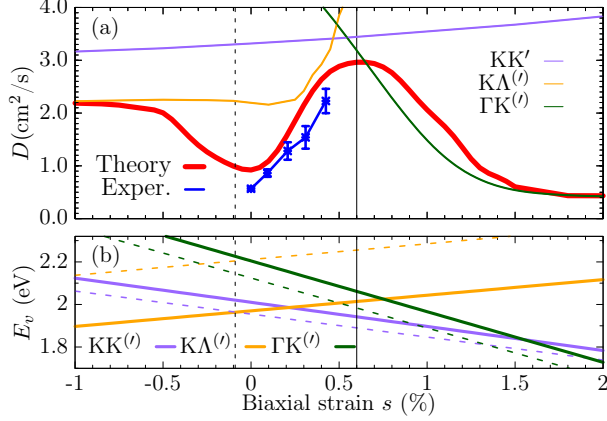


FIG. 3. **Strain-dependent stationary diffusion.** (a) Diffusion coefficient plotted as a function of biaxial strain in WS_2 containing a direct comparison between theoretically predicted (red solid line) and experimentally measured (blue line with errorbars) values. Note that the experiment was performed with uniaxial strain that has been projected to equivalent biaxial strain values (cf. supplementary material). The thin lines show the gedanken experiment where only KK' (blue), $\text{KA}^{(\prime)}$ (orange) and $\text{K}\Gamma^{(\prime)}$ (green) excitons are taken into account (besides the optically excited KK states). (b) Strain-dependent energy shifts of the minima of $\text{KK}^{(\prime)}$, $\text{KA}^{(\prime)}$ and $\text{K}\Gamma^{(\prime)}$ excitons. The dashed lines indicate the case with electrons located in equivalent primed exciton valleys. The vertical dashed line marks the strain at which $E_{\text{KA}} \approx E_{\text{KK}'}$ giving rise to a minimum in the diffusion coefficient, while the vertical solid line indicates the maximum of the diffusion.

respectively. These thin lines reflect the scenario of valley-intrinsic diffusion, where the overall diffusion is dominated by the considered specific valley and the corresponding valley-specific diffusion determined by its total mass and intravalley scattering [33]. We find immediately that the saturation value of the diffusion at compressive (tensile) strain is determined by KA ($\text{K}\Gamma$) excitons, while the maximum in diffusion is governed by the contribution of KK' exciton.

To better understand the valley-specific contribution to the overall diffusion, we show the strain dependent energy of the involved exciton valley minima in Fig. 3b [27]. We find that at larger compressive (tensile) strain values, KA ($\text{K}\Gamma^{(\prime)}$) excitons are the energetically lowest and thus most occupied states. The same applies to KK' excitons for strain values around 0.5%. As shown in our previous work [33], efficient intervalley scattering gives rise to one joint diffusion coefficient, however the weight of each

valley is determined by its relative occupation. The latter depends crucially on the position of the bottom of the valley E_v as well as on degeneracy (3 times larger for $\text{KA}^{(\prime)}$) or total mass (smaller total mass leads to smaller population): This explains why KA or the very massive $\text{K}\Gamma^{(\prime)}$ excitons still contribute even when $E_{\text{KK}'} < E_{\text{KA}}, E_{\text{K}\Gamma'}$ [see e.g. vertical solid line in Fig. 3a]. At very strong compressive strain it is KA which dominates the diffusion. Since at these strain values, the KA valley is already by far the energetically lowest state, the diffusion coefficient is not affected anymore by further strain-induced energetic changes resulting in a stationary value. The same also applies to the situation at high tensile strain, where the $\text{K}\Gamma'$ valley when low enough becomes dominant also due to its large effective mass and high exciton occupation.

The predicted maximum in the exciton diffusion at about 0.6% is formed when moving from the strain regime, where KK' excitons are energetically lowest states toward the regime governed by $\text{K}\Gamma^{(\prime)}$ states. The latter exhibit a considerably slower diffusion due to a much larger effective mass. The dip toward the unstrained case cannot be explained by just considering valley-intrinsic diffusion and is due to intervalley scattering, which will be discussed separately in the next section. Note that the abrupt increase in the diffusion coefficient in the considered hypothetical two-valley system dominated by $\text{K}\Gamma^{(\prime)}$ (thin green line) and KA (thin orange line) excitons for strain values around 0.5% is due to the increasing impact of KK excitons exhibiting a much smaller effective mass and thus a much larger diffusion coefficient [33]. The thin purple line does not show this steep increase, since KK' and KK excitons have a very similar dependence on strain modifying their separation by only approximately 5 meV per percentage of biaxial strain (cf. solid and dashed purple line in Fig. 3b).

We compare our microscopic results with measurements of the exciton diffusion in an uniaxially strained WS_2 monolayer. To this end, the monolayer is placed on a flexible PMMA substrate and a homogeneous, uniaxial, tensile strain from 0 % to 1 % is applied via the bending method [9, 14]. The similar optical properties between PMMA and SiO_2 make a comparison of experiment and theory possible. Since we apply uniaxial strain, the experimentally determined strain values are related to the biaxial ones in the theory by comparing the energy shifts of the $\text{KK}^{(\prime)}$. The exciton diffusion is measured by space- and time-resolved photoluminescence after applying a spatially localized optical excitation at 2.10 eV (see supplementary information for details). We find an

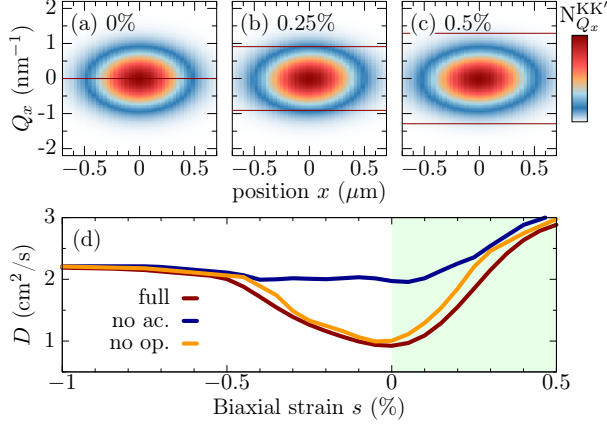


FIG. 4. **Impact of intervalley scattering.** (a)-(c) Wigner function $N_{Q_x}^v(x)$ is shown in dependence on $\mathbf{Q} \equiv (Q_x, 0)$ and $\mathbf{r} \equiv (x, 0)$ at 40 ps for the lowest $v = \text{KK}'$ valley and three different values of strain. Thin horizontal lines indicate the minimum wave-vector required for intervalley scattering via TA phonons. (d) Comparison of the full simulation (dark-red) with the cases in which only acoustic (dark-blue) or optical (orange) phonons are switched off.

excellent agreement between theoretically predicted and experimentally measured diffusion coefficients in the experimentally accessible strain region, cf. Fig. 3a. We see an increase in the diffusion coefficient from approximately 0.6 to 2.2 cm^2/s when varying the strain from 0 to 0.5%. The slope of this increase strongly depends on the formation of the minimum in the diffusion coefficient D appearing approximately for the unstrained case.

Impact of intervalley scattering: While the overall diffusion discussed so far was dominated by one exciton valley with the lowest energy and largest occupation (valley-intrinsic diffusion), there are strain regions where multiple valleys have similar energies, cf. Fig. 3b. This occurs e.g. at small compressive strain values, where KA (solid orange) and KK' excitons (dashed purple) cross, cf. the vertical dashed line. Here, intervalley scattering turns out to play a crucial role resulting in a minimum in the exciton diffusion, cf. Fig. 3a.

Now, we investigate the origin of the predicted dip in the diffusion coefficient for the unstrained WS_2 monolayer, cf. Fig. 3a. In particular, we study the role of intervalley scattering between KK' and KA excitons, whose energies are the lowest and cross in the strain region, where the minimum appears, cf. Fig. 3b. The intervalley scattering between KK' and KA excitons is driven by absorption or emission of high-momentum M phonons. These phonons can

be approximated as nearly dispersion-free including two acoustic modes with the energies of 16.5 and 22.7 meV. The corresponding optical M phonons have larger energies between 40 and 50 meV [52]. When the strain-induced separation between valleys becomes larger than these phonon energies, excitons from the energetically lowest states cannot scatter any longer out of these states, cf. Fig. 1b. To better visualize the condition for this phonon bottleneck, we show the Wigner function for the KK' excitons for three different strain values, where KK' are the energetically lowest states, cf. Figs. 4(a)-(c). Here, the thin horizontal lines show the minimum momentum $|\bar{Q}_x|$ required for the absorption of acoustic M phonons. In the unstrained case [Fig. 4a], the two momentum-dark exciton valleys are aligned [Fig. 3b], thus all intervalley channels into KA states are possible. The situation changes at 0.25% strain [Fig. 4b], where the energetic misalignment is already large enough that only a small portion of the most occupied excitons is able to scatter into KA states. At 0.5% strain [Fig. 4c], there are almost no occupied states fulfilling the condition for intervalley scattering resulting in a phonon bottleneck.

Now we address the impact of this phonon bottleneck for the strain-dependent evolution of the exciton diffusion. In Fig. 4d, we compare the full calculation (also shown in Fig. 3a) with the case, where the KK' - KA intervalley scattering via acoustic or optical phonons is switched off, respectively. We see that optical phonons have in general a minor effect, since their energy is relatively high resulting in a small phonon occupation and thus a negligibly small phonon absorption. We also find that scattering with acoustic phonons does not play a role for strain values $|s| \gtrsim 0.5\%$. The reason is the phonon bottleneck illustrated in Fig. 4c. However, in the strain region $|s| \lesssim 0.5\%$, switching off scattering with acoustic phonons suppresses the appearance of the dip in the exciton diffusion. This illustrates the crucial role of intervalley scattering with acoustic phonons for the formation of the predicted minimal exciton diffusion in unstrained WS_2 monolayers.

Note that the scattering with M phonons connecting KK' and KA excitons is particularly strong according to DFT calculations [52]. In contrast, the corresponding phonon-induced intervalley scattering connecting $\Gamma\text{K}^{(\prime)}$ and $\text{KK}^{(\prime)}$ excitons is much weaker. This together with the much larger effective mass and smaller diffusion coefficient in the $\Gamma\text{K}^{(\prime)}$ valley does not lead to a similar dip in the exciton diffusion around 1.5% strain, where KK' - and $\Gamma\text{K}^{(\prime)}$ states are energetically lowest and cross [Fig. 3b]. Note that

the efficiency of the KK' - KA intervalley scattering together with the small energy of acoustic M phonon leads to a persistence of the dip also at smaller temperatures, as shown in the supplementary material.

Finally, we briefly discuss the strain-dependence of exciton diffusion in other TMD materials. While the physical mechanisms are the same, in Mo-based monolayers one needs a larger tensile or compressive strain to reach the multi-valley features discussed for WS_2 . In particular, the situation in MoS_2 is more involved due to the initial excitonic landscape in the unstrained case, where the position of $E_{TK(\prime)}$ strongly depends on the relative distance $\Delta E_{K\Gamma}$ of the valence-band maxima located in K and Γ . The latter is still being controversially discussed in literature [27, 36, 53, 54]. We predict a qualitatively different strain-dependent exciton diffusion in MoS_2 depending on $\Delta E_{K\Gamma}$, cf. the supplementary material. An experimental study of exciton diffusion in MoS_2 could thus provide a better understanding of the relative position of the bright KK and the dark $\Gamma K^{(\prime)}$ excitons.

II. DISCUSSION

In conclusion, the presented joint theory-experiment study provides new microscopic insights into strain-dependent exciton diffusion in TMD monolayers. We find that the diffusion becomes faster or slower with strain in a non-trivial and non-monotonic way. This is a result of the interplay between lattice-distortions and the remarkable multi-

valley excitonic landscape in TMDs. Strain-induced shifts of exciton energies change the relative energy separations in the excitonic landscape of bright and momentum-dark excitons. This has an immediate impact on which state is dominant and governs the overall diffusion coefficient. In particular, we predict a dip in the diffusion for unstrained WS_2 monolayers that we microscopically ascribe to intervalley scattering with acoustic phonons. This dip is followed by a large increase of exciton diffusion by a factor of 3 for tensile biaxial strain of up to 0.6%. The theoretical prediction is found to be in excellent agreement with spatiotemporal photoluminescence experiments. Overall, our study provides microscopic insights into the impact of strain on exciton diffusion in technologically promising 2D materials and uncovers the underlying fundamental intra- and intervalley scattering processes involving bright and momentum-dark excitons.

Supporting Information

Additional details on microscopic modeling and measurements on strain-dependent exciton diffusion are included. Furthermore, temperature dependence as well as exciton diffusion in different strained TMD monolayers are discussed.

Acknowledgements: This project has received funding from the Swedish Research Council (VR, project number 2018-00734) and the European Unions Horizon 2020 research and innovation programme under grant agreement no. 881603 (Graphene Flagship). The authors thank Zahra Khatibi and Maja Feierabend for fruitful discussions.

-
- [1] G. Wang, A. Chernikov, M. M. Glazov, T. F. Heinz, X. Marie, T. Amand, and B. Urbaszek, Colloquium: Excitons in atomically thin transition metal dichalcogenides, *Rev. Mod. Phys.* **90**, 021001 (2018).
 - [2] T. Mueller and E. Malic, Exciton physics and device application of two-dimensional transition metal dichalcogenide semiconductors, *npj 2D Mater. and Applications* **2**, 29 (2018).
 - [3] E. Malic, M. Selig, M. Feierabend, S. Brem, D. Christiansen, F. Wendler, A. Knorr, and G. Berghäuser, Dark excitons in transition metal dichalcogenides, *Phys. Rev. Mater.* **2**, 014002 (2018).
 - [4] K. F. Mak, C. Lee, J. Hone, J. Shan, and T. F. Heinz, Atomically thin MoS_2 : A new direct-gap semiconductor, *Phys. Rev. Lett.* **105**, 136805 (2010).
 - [5] A. Chernikov, T. C. Berkelbach, H. M. Hill, A. Rigosi, Y. Li, O. B. Aslan, D. R. Reichman, M. S. Hybertsen, and T. F. Heinz, Exciton binding energy and nonhydrogenic rydberg series in monolayer WS_2 , *Phys. Rev. Lett.* **113**, 076802 (2014).
 - [6] J. Kunstmann, F. Mooshammer, P. Nagler, A. Chaves, F. Stein, N. Paradiso, G. Plechinger, C. Strunk, C. Schüller, G. Seifert, D. R. Reichman, and T. Korn, Momentum-space indirect interlayer excitons in transition-metal dichalcogenide van der waals heterostructures, *Nat. Phys.* **14**, 801 (2018).
 - [7] P. Merkl, F. Mooshammer, P. Steinleitner, A. Girnghuber, K.-Q. Lin, P. Nagler, J. Holler, C. Schüller, J. M. Lupton, T. Korn, S. Ovesen, S. Brem, E. Malic, and R. Huber, Ultrafast transition between exciton phases in van der waals heterostructures, *Nat. Mater.* **18**, 691 (2019).
 - [8] S. Brem, K.-Q. Lin, R. Gillen, J. M. Bauer,

- J. Maultzsch, J. M. Lupton, and E. Malic, Hybridized intervalley moiré excitons and flat bands in twisted WSe₂ bilayers, *Nanoscale* **12**, 11088 (2020).
- [9] R. Schmidt, I. Niehues, R. Schneider, M. Drüppel, T. Deilmann, M. Rohlfing, S. M. de Vasconcellos, A. Castellanos-Gomez, and R. Bratschitsch, Reversible uniaxial strain tuning in atomically thin WSe₂, *2D Mater.* **3**, 021011 (2016).
- [10] H. J. Conley, B. Wang, J. I. Ziegler, R. F. Haglund, S. T. Pantelides, and K. I. Bolotin, Bandgap engineering of strained monolayer and bilayer MoS₂, *Nano Lett.* **13**, 3626 (2013).
- [11] K. He, C. Poole, K. F. Mak, and J. Shan, Experimental demonstration of continuous electronic structure tuning via strain in atomically thin MoS₂, *Nano Lett.* **13**, 2931 (2013).
- [12] G. Plechinger, A. Castellanos-Gomez, M. Buscema, H. S. J. van der Zant, G. A. Steele, A. Kuc, T. Heine, C. Schüller, and T. Korn, Control of biaxial strain in single-layer molybdenite using local thermal expansion of the substrate, *2D Mater.* **2**, 015006 (2015).
- [13] R. Frisenda, M. Drüppel, R. Schmidt, S. Michaelis de Vasconcellos, D. Perez de Lara, R. Bratschitsch, M. Rohlfing, and A. Castellanos-Gomez, Biaxial strain tuning of the optical properties of single-layer transition metal dichalcogenides, *npj 2D Mater. and Applications* **1**, 10 (2017).
- [14] I. Niehues, R. Schmidt, M. Drüppel, P. Maruhn, D. Christiansen, M. Selig, G. Berghäuser, D. Wigger, R. Schneider, L. Braasch, R. Koch, A. Castellanos-Gomez, T. Kuhn, A. Knorr, E. Malic, M. Rohlfing, S. Michaelis de Vasconcellos, and R. Bratschitsch, Strain control of exciton-phonon coupling in atomically thin semiconductors, *Nano Lett.* **18**, 1751 (2018).
- [15] G.-H. Peng, P.-Y. Lo, W.-H. Li, Y.-C. Huang, Y.-H. Chen, C.-H. Lee, C.-K. Yang, and S.-J. Cheng, Distinctive signatures of the spin- and momentum-forbidden dark exciton states in the photoluminescence of strained WSe₂ monolayers under thermalization, *Nano Lett.* **19**, 2299 (2019).
- [16] L. Mennel, V. Smejkal, L. Linhart, J. Burgdörfer, F. Libisch, and T. Mueller, Band nesting in two-dimensional crystals: An exceptionally sensitive probe of strain, *Nano Lett.* **20**, 4242 (2020).
- [17] P. Tonndorf, R. Schmidt, R. Schneider, J. Kern, M. Buscema, G. A. Steele, A. Castellanos-Gomez, H. S. J. van der Zant, S. M. de Vasconcellos, and R. Bratschitsch, Single-photon emission from localized excitons in an atomically thin semiconductor, *Optica* **2**, 347 (2015).
- [18] J. Kern, I. Niehues, P. Tonndorf, R. Schmidt, D. Wigger, R. Schneider, T. Stiehm, S. Michaelis de Vasconcellos, D. E. Reiter, T. Kuhn, and R. Bratschitsch, Nanoscale positioning of single-photon emitters in atomically thin WSe₂, *Adv. Mater.* **28**, 7101 (2016).
- [19] C. Palacios-Berraquero, D. M. Kara, A. R.-P. Montblanch, M. Barbone, P. Latawiec, D. Yoon, A. K. Ott, M. Loncar, A. C. Ferrari, and M. Atatüre, Large-scale quantum-emitter arrays in atomically thin semiconductors, *Nat. Commun.* **8**, 15093 (2017).
- [20] A. Branny, S. Kumar, R. Proux, and B. D. Gerardot, Deterministic strain-induced arrays of quantum emitters in a two-dimensional semiconductor, *Nat. Commun.* **8**, 15053 (2017).
- [21] M. R. Rosenberger, C. K. Dass, H.-J. Chuang, S. V. Sivaram, K. M. McCreary, J. R. Hendrickson, and B. T. Jonker, Quantum calligraphy: Writing single-photon emitters in a two-dimensional materials platform, *ACS Nano* **13**, 904 (2019).
- [22] A. V. Tyurnina, D. A. Bandurin, E. Khestanova, V. G. Kravets, M. Koperski, F. Guinea, A. N. Grigorenko, A. K. Geim, and I. V. Grigorieva, Strained bubbles in van der waals heterostructures as local emitters of photoluminescence with adjustable wavelength, *ACS Photonics* **6**, 516 (2019), <https://doi.org/10.1021/acsp Photonics.8b01497>.
- [23] C. Carmesin, M. Lorke, M. Florian, D. Erben, A. Schulz, T. O. Wehling, and F. Jahnke, Quantum-dot-like states in molybdenum disulfide nanostructures due to the interplay of local surface wrinkling, strain, and dielectric confinement, *Nano Lett.* **19**, 3182 (2019).
- [24] M. G. Harats, J. N. Kirchhof, M. Qiao, K. Greben, and K. I. Bolotin, Dynamics and efficient conversion of excitons to trions in non-uniformly strained monolayer WS₂, *Nat. Photonics* **14**, 324 (2020).
- [25] J. Feng, X. Qian, C.-W. Huang, and J. Li, Strain-engineered artificial atom as a broad-spectrum solar energy funnel, *Nat. Photonics* **6**, 866 (2012).
- [26] A. Steinhoff, M. Rösner, F. Jahnke, T. O. Wehling, and C. Gies, Influence of excited carriers on the optical and electronic properties of MoS₂, *Nano Lett.* **14**, 3743 (2014).
- [27] Z. Khatibi, M. Feierabend, M. Selig, S. Brem, C. Linderälv, P. Erhart, and E. Malic, Impact of strain on the excitonic linewidth in transition metal dichalcogenides, *2D Mater.* **6**, 015015 (2018).
- [28] M. Feierabend, A. Morlet, G. Berghäuser, and E. Malic, Impact of strain on the optical fingerprint of monolayer transition-metal dichalcogenides, *Phys. Rev. B* **96**, 045425 (2017).
- [29] D. F. Cordovilla Leon, Z. Li, S. W. Jang, C.-H. Cheng, and P. B. Deotare, Exciton transport in strained monolayer WSe₂, *Appl. Phys. Lett.* **113**, 252101 (2018), <https://doi.org/10.1063/1.5063263>.
- [30] Q. H. Wang, K. Kalantar-Zadeh, A. Kis, J. N. Coleman, and M. S. Strano, Electronics and optoelectronics of two-dimensional transition metal dichalcogenides, *Nat. Nanotechnol.* **7**, 699 (2012).
- [31] K. F. Mak and J. Shan, Photonics and optoelectronics of 2D semiconductor transition metal dichalcogenides, *Nat. Photonics* **10**, 216 (2016).
- [32] D. Unuchek, A. Ciarrocchi, A. Avsar, K. Watanabe, T. Taniguchi, and A. Kis, Room-temperature

- electrical control of exciton flux in a van der waals heterostructure, *Nature* **560**, 340 (2018).
- [33] R. Rosati, R. Perea-Causín, S. Brem, and E. Malic, Negative effective excitonic diffusion in monolayer transition metal dichalcogenides, *Nanoscale* **12**, 356 (2020).
- [34] J. Zipfel, M. Kulig, R. Perea-Causín, S. Brem, J. D. Ziegler, R. Rosati, T. Taniguchi, K. Watanabe, M. M. Glazov, E. Malic, and A. Chernikov, Exciton diffusion in monolayer semiconductors with suppressed disorder, *Phys. Rev. B* **101**, 115430 (2020).
- [35] R. Perea-Causín, S. Brem, R. Rosati, R. Jago, M. Kulig, J. D. Ziegler, J. Zipfel, A. Chernikov, and E. Malic, Exciton propagation and halo formation in two-dimensional materials, *Nano Lett.* **19**, 7317 (2019).
- [36] A. Kormányos, G. Burkard, M. Gmitra, J. Fabian, V. Zólyomi, N. D. Drummond, and V. Fal'ko, k-p theory for two-dimensional transition metal dichalcogenide semiconductors, *2D Mater.* **2**, 022001 (2015).
- [37] H. Haug and S. W. Koch, *Quantum Theory of the Optical and Electronic Properties of Semiconductors: Fifth Edition* (World Scientific Publishing Company, 2009).
- [38] M. Selig, G. Berghäuser, A. Raja, P. Nagler, C. Schüller, T. F. Heinz, T. Korn, A. Chernikov, E. Malic, and A. Knorr, Excitonic linewidth and coherence lifetime in monolayer transition metal dichalcogenides, *Nat. Commun.* **7**, 13279 (2016).
- [39] M. Selig, G. Berghuser, M. Richter, R. Bratschitsch, A. Knorr, and E. Malic, Dark and bright exciton formation, thermalization, and photoluminescence in monolayer transition metal dichalcogenides, *2D Mater.* **5**, 035017 (2018).
- [40] S. Brem, M. Selig, G. Berghäuser, and E. Malic, Exciton relaxation cascade in two-dimensional transition metal dichalcogenides, *Sci. Rep.* **8**, 8238 (2018).
- [41] S. Brem, J. Zipfel, M. Selig, A. Raja, L. Waldecker, J. D. Ziegler, T. Taniguchi, K. Watanabe, A. Chernikov, and E. Malic, Intrinsic lifetime of higher excitonic states in tungsten diselenide monolayers, *Nanoscale* **11**, 12381 (2019).
- [42] O. Hess and T. Kuhn, Maxwell-bloch equations for spatially inhomogeneous semiconductor lasers. i. theoretical formulation, *Phys. Rev. A* **54**, 3347 (1996).
- [43] R. Jago, R. Perea-Causín, S. Brem, and E. Malic, Spatio-temporal dynamics in graphene, *Nanoscale* **11**, 10017 (2019).
- [44] S. Brem, A. Ekman, D. Christiansen, F. Katsch, M. Selig, C. Robert, X. Marie, B. Urbaszek, A. Knorr, and E. Malic, Phonon-assisted photoluminescence from indirect excitons in monolayers of transition-metal dichalcogenides, *Nano Lett.* **20**, 2849 (2020).
- [45] A. M. Dadgar, D. Scullion, K. Kang, D. Esposito, E. H. Yang, I. P. Herman, M. A. Pimenta, E.-J. G. Santos, and A. N. Pasupathy, Strain engineering and raman spectroscopy of monolayer transition metal dichalcogenides, *Chem. Mater.* **30**, 5148 (2018).
- [46] O. B. Aslan, M. Deng, and T. F. Heinz, Strain tuning of excitons in monolayer WSe₂, *Phys. Rev. B* **98**, 115308 (2018).
- [47] O. B. Aslan, M. Deng, M. L. Brongersma, and T. F. Heinz, Strained bilayer WSe₂ with reduced exciton-phonon coupling, *Phys. Rev. B* **101**, 115305 (2020).
- [48] T. Kato and T. Kaneko, Transport dynamics of neutral excitons and trions in monolayer WS₂, *ACS Nano* **10**, 9687 (2016).
- [49] F. Cadiz, C. Robert, E. Courtade, M. Manca, L. Martinelli, T. Taniguchi, K. Watanabe, T. Amand, A. C. H. Rowe, D. Paget, B. Urbaszek, and X. Marie, Exciton diffusion in WSe₂ monolayers embedded in a van der waals heterostructure, *Appl. Phys. Lett.* **112**, 152106 (2018), <https://doi.org/10.1063/1.5026478>.
- [50] J. He, D. He, Y. Wang, Q. Cui, F. Ceballos, and H. Zhao, Spatiotemporal dynamics of excitons in monolayer and bulk WS₂, *Nanoscale* **7**, 9526 (2015).
- [51] M. Kulig, J. Zipfel, P. Nagler, S. Blanter, C. Schüller, T. Korn, N. Paradiso, M. M. Glazov, and A. Chernikov, Exciton diffusion and halo effects in monolayer semiconductors, *Phys. Rev. Lett.* **120**, 207401 (2018).
- [52] Z. Jin, X. Li, J. T. Mullen, and K. W. Kim, Intrinsic transport properties of electrons and holes in monolayer transition-metal dichalcogenides, *Phys. Rev. B* **90**, 045422 (2014).
- [53] Y. Uchiyama, A. Kutana, K. Watanabe, T. Taniguchi, K. Kojima, T. Endo, Y. Miyata, H. Shinohara, and R. Kitaura, Momentum-forbidden dark excitons in hbn-encapsulated monolayer MoS₂, *npj 2D Mater. and Applications* **3**, 26 (2019).
- [54] T. Deilmann and K. S. Thygesen, Finite-momentum exciton landscape in mono- and bilayer transition metal dichalcogenides, *2D Mater.* **6**, 035003 (2019).

Supporting Information:

Strain-dependent exciton diffusion in transition metal dichalcogenides

R. Rosati¹, S. Brem¹, R. Perea-Causín¹, Robert Schmidt², Iris Niehues², Steffen Michaelis de Vasconcellos², Rudolf Bratschitsch², and Ermin Malic¹

¹*Chalmers University of Technology, Department of Physics, 412 96 Gothenburg, Sweden*

²*Institute of Physics and Center for Nanotechnology, University of Münster, 48149 Münster, Germany*

August 20, 2020

1 Wannier equation and exciton-phonon scattering

The energetic position of the excitonic energies E_v is given by $E_v = E_v^0 - E_v^b$, where E_v^0 is the single-particle separation between top of the valence band in the K and Γ valley and bottom of the conduction band in the K, K' and Λ valleys for $v = \text{KK}^{(\prime)}$, $\text{K}\Lambda^{(\prime)}$, $\Gamma\text{K}^{(\prime)}$. The exciton binding energy E_v^b is obtained from the solution of the Wannier equation

$$\frac{\hbar^2 k^2}{2m_v} \Psi_v(\mathbf{k}) - \sum_{\mathbf{q}} W_{\mathbf{q}} \Psi_v(\mathbf{k} + \mathbf{q}) = E_v^0 \Psi_v(\mathbf{k}) \quad , \quad (1)$$

where m_v is the reduced exciton mass in valley v , i.e. $1/m_v = 1/m_v^e + 1/m_v^h$ with $m^{e,h}$ denoting the effective mass of electrons and holes in the excitonic valley v . Here, m_v and E_v^0 crucially depend on strain. We take the starting parameters for the unstrained single-particle dispersion from Ref. [1] and use the strain-dependent variation of single-particle parameters provided in Ref. [2]. Furthermore, $\Psi_v(\mathbf{k})$ appearing in Eq. (1) is the excitonic wave function in momentum space, while $W_{\mathbf{q}}$ is the Coulomb interaction, for which we have used a modified form of the potential for charges in a thin film of thickness d surrounded by a dielectric environment [3]. Taking into account anisotropic dielectric tensors and solving the Poisson equation with the boundary conditions described above yields $W_q = V_q/\epsilon_{scr}(q)$ with the bare 2D-Fourier transformed Coulomb potential V_q and a non-local screening $\epsilon_{scr}(q) = \kappa_1 \tanh \left[\frac{1}{2} \left[\alpha_1 dq - \ln \left(\frac{\kappa_1 - \kappa_2}{\kappa_1 + \kappa_2} \right) \right] \right]$, where $\kappa_i = \sqrt{\epsilon_i^{\parallel} \epsilon_i^{\perp}}$ and $\alpha_i = \sqrt{\epsilon_i^{\parallel} / \epsilon_i^{\perp}}$ account for the parallel and perpendicular component of the dielectric tensor ϵ_i of monolayer ($i = 1$) and environment ($i = 2$), whose parameters have been taken from Refs. [4] and [5], respectively. In this work, we consider the intrinsic undoped regime, where the effect of trions [6–9] is negligible. Moreover, we focus on intrinsic excitonic properties, hence we disregard defects/disorders, which are expected to lead to a quantitative slow-down of the overall propagation without affecting qualitatively the strain dependence. Finally, we also neglect the impact of spin-dark states [8, 10], which are known to appear in PL spectra under certain conditions, but since

they have similar properties as KK' excitons (in terms of dispersion relation), they are expected to only lead to quantitative changes.

The scattering-induced dynamics for the Wigner function can be written as $\dot{N}_{\mathbf{Q}}^v(\mathbf{r}, t)\Big|_{sc} = \Gamma_{\mathbf{Q}}^{\text{in},v}(\mathbf{r}, t) - \Gamma_{\mathbf{Q}}^{\text{out},v} N_{\mathbf{Q}}(\mathbf{r}, t)$, where $\Gamma_{\mathbf{Q}}^{\text{in},v}(\mathbf{r}, t) = \sum_{\mathbf{Q}',v'} \Gamma_{\mathbf{Q}\mathbf{Q}'}^{vv'} N_{\mathbf{Q}'}^{v'}(\mathbf{r}, t)$ and $\Gamma_{\mathbf{Q}}^{\text{out},v} = \sum_{\mathbf{Q}',v'} \Gamma_{\mathbf{Q}'\mathbf{Q}}^{v'v}$. The scattering rates $\Gamma_{\mathbf{Q}\mathbf{Q}'}^{vv'}$ of the exciton-phonon coupling read in second-order Born-Markov approximation [11,12]

$$\Gamma_{\mathbf{Q}\mathbf{Q}'}^{vv'} = \frac{2\pi}{\hbar} \sum_{\xi\pm} \left| G_{\xi|\mathbf{Q}'-\mathbf{Q}+\mathbf{Q}'_v, -\mathbf{Q}_v}^{vv'} \right|^2 \left(n_{\xi, \mathbf{Q}'-\mathbf{Q}+\mathbf{Q}'_v, -\mathbf{Q}_v} + \frac{1}{2} \pm \frac{1}{2} \right) \delta \left(\epsilon_{\alpha} \pm \hbar\omega_{\xi, \mathbf{Q}'-\mathbf{Q}+\mathbf{Q}'_v, -\mathbf{Q}_v} - \epsilon_{\alpha'} \right) ,$$

where $\epsilon_{\alpha(v)} \equiv E_{v(v)} + \hbar^2|\mathbf{Q}^{(v)}|^2/2M_{v(v)}$ and \mathbf{Q}_v addresses the position in the Brillouin zone of the bottom of valley v , \pm refers to emission/absorption of phonons, ξ labels the phonon modes, $\hbar\omega_{\xi\mathbf{q}}$ provides the energy of phonon ξ with momentum \mathbf{q} and $n_{\xi, \mathbf{q}}$ describes the equilibrium phonon distribution. We take into account longitudinal and transverse acoustic (LA, TA) and optical (LO, TO) modes as well as the out-of-plane A_1 optical mode, which provide the most efficient scattering channels [13]. The exciton-phonon scattering coefficients G can be written as [3] $\left| G_{\xi\mathbf{q}}^{vv'} \right|^2 = \sum_{p=e,h} \left| g_{p\xi\mathbf{q}}^{vv'} \mathcal{F}_p^{vv'}(\mathbf{q}) \right|^2$, where p distinguishes between electrons/holes, \mathcal{F} is the form factor $\mathcal{F}_p^{vv'}(\mathbf{q}) = \sum_{\mathbf{k}} \Psi_{v'}^*(\mathbf{k}) \Psi_v(\mathbf{k} + \alpha_v^p \mathbf{q})$, with $\alpha_v^p = (m_v^e + m_v^h)^{-1} \left[\pm m_v^{h/e} \right]$ for $p = e, h$, respectively, while g are the carrier-phonon scattering coefficients which are approximated with the generic form of a deformation potential $g_{p\xi\mathbf{q}}^{vv'} = \sqrt{\frac{\hbar}{2\rho A \omega_{\xi\mathbf{q}}}} \mathcal{D}_{p\xi\mathbf{q}}$. Here, ρ denotes the surface mass density of the monolayer (whose small variations with strain have been omitted) and A the area of the system. For the coupling constant $\mathcal{D}_{p\xi\mathbf{q}}$ we adopt the approximations deduced from DFPT calculations in Ref. [13], where long range acoustic phonons couple linear in momentum $\mathcal{D}_{\xi\mathbf{q}} \equiv \mathcal{D}_{\xi}^{(1)} q$, while optical phonons and short range acoustic modes couple with a constant strength $\mathcal{D}_{\xi\mathbf{q}} \equiv \mathcal{D}_{\xi}^{(0)}$ in the vicinity of high symmetry points. The phonon energies as well as deformation constants $\mathcal{D}^{(0)}$ and $\mathcal{D}^{(1)}$ for all possible intra and intervalley scattering channels are listed in Ref. [13], including longitudinal and transverse acoustic (LA, TA) and optical (LO, TO) modes as well as the out-of-plane A_1 optical mode. Finally, for describing the radiative decay [3,14] we use $\gamma = 4.5$ meV in accordance to a recombination-induced broadening of the linewidth of 4.5 meV in FWHM [2]. We find, however, that the radiative recombination rate has a negligible role on the qualitative aspects of the investigated effective diffusion in h-BN encapsulated WS_2 monolayers [15]. For the same reason we have also neglected strain-induced changes of γ , which are typically weak [2,16].

2 Exciton diffusion in WS_2 at lower temperatures

We study the impact of temperature on the predicted dip in the exciton diffusion for unstrained WS_2 , cf. Fig. 3(a) in the main text. A decrease in temperature is accompanied by a spectral shift of excitonic resonances, often described via the Varshni equation [17]. The shift originates from an interplay of temperature-induced changes in the electron-phonon interaction (polaron shift) and a lattice contraction at smaller temperature. We denote the latter effect as temperature-induced strain s_T . To which extent the shift is due to one or the other contribution is still under debate in literature, see e.g. [18] and references therein. This goes beyond the scope of the present work. For the moment, we neglect this effect, i.e. $s_T = 0$, and we show the exciton diffusion as a function

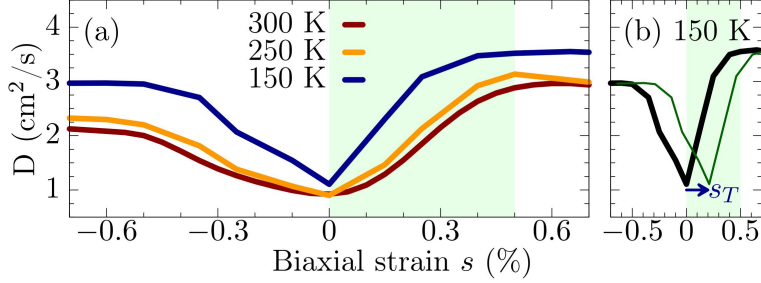


Figure 1: **Impact of temperature.** (a) Strain-dependent stationary diffusion coefficients at different temperatures and (b) at 150 K assuming an additional background strain s_T due to the lattice contraction at smaller temperatures. The green-shaded area indicates the experimentally accessible strain region at room temperature.

of temperature in Fig. 1(a). We find that the predicted dip in the diffusion becomes narrower for decreasing temperatures. This can be easily explained by studying Figs. 4(a)-(c) in the main manuscript: While the position of the thin red line is assumed independent of temperature, the width of the exciton occupation in momentum space decreases with temperature. As a result, at smaller temperatures already at $s = 0.25\%$ the intervalley scattering via absorption of TA modes is suppressed due to a narrower distribution in momentum, and at this strain value the corresponding dip already saturates, as shown in Fig. 1(a).

Interestingly, the minimum of the dip at $s \approx 0\%$ seems independent of temperature. To understand this we study the diffusion coefficient from the Fick's law by considering only one phonon mode and assuming $\tau_Q \equiv \tau_{\text{ph}}$. The resulting diffusion $D_{\text{ph}} \equiv \tau_{\text{ph}} k_B T / M$ behaves with temperature as $D_{\text{ph}} \propto \text{Exp}\left(\frac{\hbar\omega_{\text{ph}}}{k_B T}\right) T \equiv f_{\text{ph}}(T)$. In the range of temperatures between 150 and 300 K f_{TA} varies weakly. This is not the case anymore when considering more energetic phonon modes. Here, f_{TO} would increase at smaller temperatures, as expected from the naive consideration that weaker scattering leads to a faster diffusion. Since acoustic phonons are crucial for the generation of the dip (as discussed in the main manuscript), we have an almost temperature-independent dip minimum in the considered temperature range.

Finally, in Fig. 1(b) we consider a non-zero background strain s_T such that it gives rise to the half of the observed temperature-induced shift [19]. This results in a shift of the dip in the exciton diffusion to higher strain values. This means that the non-monotonicity appears in the strain range that is experimentally accessible at room temperature. Although with state-of-the-art techniques it is complicated to induce strain at smaller temperatures, Fig. 1(b) predicts that the interplay between temperature-induced lattice shrinking and additional strain could in principle lead to observations of a pronounced dip in the exciton diffusion also at experimentally accessible tensile strain values.

3 Exciton diffusion in other TMDs

We now briefly discuss the impact of strain on exciton diffusion in other TMD materials than discussed in the main manuscript. In MoS₂, the separation between the valence-band maxima located at the Γ and the K valley is still being debated in literature, cf. [1, 2, 20, 21]. Assuming a

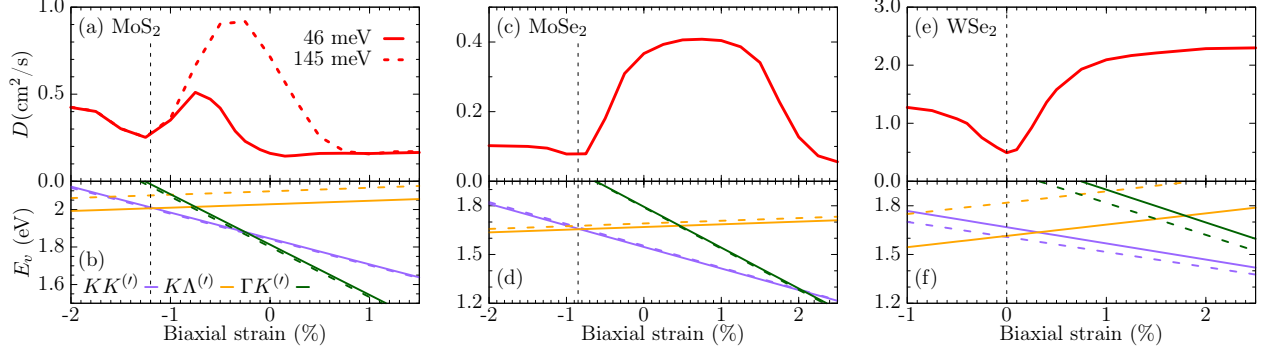


Figure 2: **Strain-dependent stationary diffusion in MoS₂, MoSe₂, and WSe₂.** The same plot as in Fig. 3 in the main manuscript. In panel (a), two different values for the separation between the higher-lying valence-band maximum in the K valley and the lower-lying one in the Γ valley have been considered, i.e. 46 meV [1] (solid line) and 145 meV [2] (dashed line). In panel (b) the smaller value has been considered.

small separation of 46 meV [1], we find that already at $s \approx 0$ the diffusion is saturated, cf. the solid line in Fig. 2(a). This can be led back to the vicinity of the Γ and the K valley in the single-particle dispersion for the unstrained case, reflecting the close position of the excitonic energies shown in Fig. 2(b). As a consequence, for tensile strain almost all excitons are located in the $\Gamma K^{(\prime)}$ state. This means that the exciton diffusion is almost unchanged for experimentally accessible strain values between 0 and 0.5%. The behaviour is more involved for compressive strain, where we observe the maximum in the region where KK' excitons are clearly energetically lowest states. Exciton diffusion further decreases for higher values of compressive strain, i.e. moving toward the regime, where $KA^{(\prime)}$ excitons are dominant.

The situation for tensile strain $\lesssim 1\%$ values changes, if a larger Γ -K separation is assumed. A value of 145 meV [2] leads to a decrease of the diffusion coefficient upon increase of strain, cf. the dashed red line in Fig. 2(a). This occurs in view of the larger separation between $E_{\Gamma K^{(\prime)}}$ and $E_{KK^{(\prime)}}$ with the former being now able to affect the overall diffusion only if larger values of strain are applied. The increased separation also affects the maximum value of the diffusion as obtained for small compressive strain, which is now approximately two times larger than in the case of the smaller separation, again reflecting a smaller contribution stemming from the dark ΓK and $\Gamma K'$ excitons.

For MoSe₂, exciton diffusion also changes only weakly for small tensile strain (Fig. 2(c)), however the microscopic origin is very different w.r.t. the solid line in Fig. 2(a), as can be seen in the excitonic energies shown in Fig. 2(d). At around 0%, KK' excitons are energetically lowest states and dominate the diffusion. Only at larger tensile strain values ($s \approx 2\%$) $\Gamma K^{(\prime)}$ excitons become dominant giving rise to a decrease of the diffusion coefficient - similar to the behaviour at slightly smaller tensile strain discussed for WS₂ in the main manuscript. Note that in the strain regimes where the overall diffusion is dominated by $KK^{(\prime)}$ the absolute value of the diffusion coefficient is much smaller than in the analogous situation in WS₂ [see maximum at 0.6% of Fig. 3(a) of the main manuscript], reflecting in particular a much stronger effectiveness of the exciton-phonon scattering with intravalley modes in MoSe₂ w.r.t. WS₂ [2].

Finally, we find that WSe₂ has a similar strain behaviour as WS₂ for compressive strain and

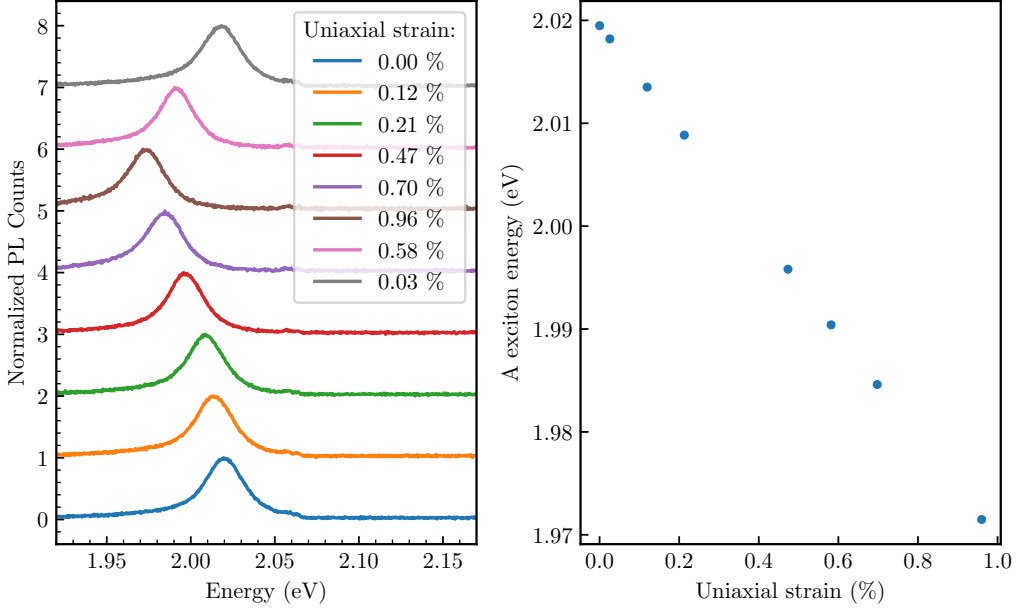


Figure 3: **Photoluminescence of the WS₂ monolayer under uniaxial tensile strain.** (a) Measured photoluminescence spectra for different uniaxial strain values. (b) Strain-dependent A exciton energies extracted from (a).

small tensile strain values, cf. Fig. 2(e). However, the decrease of the diffusion coefficient at larger tensile strain does not take place due to different energy positions of $E_{\Gamma K^{(v)}}$ and $E_{KK^{(v)}}$, Fig. 2(f).

4 Experimental determination of the diffusion coefficients of strained WS₂ monolayers

4.1 Strained WS₂ monolayers

To investigate the exciton diffusion in strained WS₂, a monolayer is mechanically exfoliated onto a Polymethyl methacrylate (PMMA) substrate (Röhme GmbH Plexiglas 0F058) of 0.5 mm thickness. By bending the substrate, the monolayer on top is uniaxially strained by up to 0.96 % [22]. Excellent strain transfer is verified by the observed red-shift of the photoluminescence (Fig. 3) with a gauge factor of 50 meV/%. To directly compare the experimental and theoretical data, the experimental uniaxial strain values have to be related to the biaxial values from the theory. Both uniaxial and biaxial tensile strain cause similar energetic shifts of the excitonic transitions, and only their gauge factors differ. For exciton diffusion, the relative energetic shift of excitonic transitions is the relevant parameter. Therefore, those experimental uniaxial strain values correspond to the theoretical biaxial ones, which yield the same exciton shift. To this end, the experimental strain values are multiplied by the ratio of the measured uniaxial gauge factor and the calculated biaxial

gauge factor [cf. Fig. 3(b)]

$$\frac{\alpha_{\text{uniaxial}}}{\alpha_{\text{biaxial}}} = \frac{50 \text{ meV}/\%}{113 \text{ meV}/\%} = 0.44. \quad (2)$$

In this way, the experimental and theoretical gauge factors match, i.e. the experiment spans a biaxial strain range from 0 % to 0.42 %.

4.2 Exciton diffusion measurement and analysis

To measure exciton diffusion, the monolayer is optically excited using 250 fs pulses at 2.10 eV from a 40 MHz femtosecond fiber laser system [23]. The monolayer PL is measured in a transmission microscope using a 50x (NA = 0.55) objective lens for excitation, resulting in a focus size of 700 nm at the sample. For detection, we use a 100x (NA = 0.9) objective lens. A streak camera (Hamamatsu C10910-05) detects the photoluminescence with a temporal resolution in the picosecond range. The detection spot of the PL can be scanned across the sample by moving the detection objective lens. The residual pump light is blocked using a long-pass filter at 2.07 eV. From the measurement we reconstruct an image sequence of the spatial distribution of the monolayer photoluminescence with a temporal resolution of ≈ 5 ps and a temporal range of up to 2 ns (Fig. 4).

Kulig et al. [24] have demonstrated that exciton diffusion in monolayer WS₂ depends on the excitation density, except for very low powers in the nanowatt regime. For higher powers, so-called “halos” are observable in the exciton photoluminescence. To be able to observe the impact of strain on diffusion coefficients predicted by the theory, exciton diffusion has to be measured in the regime, where it is independent of the excitation density.

We use two different approaches to measure exciton diffusion. In the first, we are in the excitation regime, where exciton diffusion shows the formation of halos (excitation power 2 μ W). In this case, excitons are quickly pushed away from the irradiated into a pristine area of the substrate, where they can diffuse freely.

The experimental data is fitted using a donut-like function (Fig. 4):

$$I_{\text{PL}}(x, y) = A_0 \cdot \left(e^{-((x-x_0)^2+(y-y_0)^2-d/2)^2/2\sigma^2} + e^{-((x-x_0)^2+(y-y_0)^2+d/2)^2/2\sigma^2} \right) \quad (3)$$

Here, I_{PL} is the intensity of the photoluminescence at the specific coordinate, x_0 and y_0 denote the center of the donut, A_0 the amplitude, d the diameter and σ the width of the ring. In this excitation regime, exciton transport consists of an excitation density-dependent part, creating the halo and the density-independent exciton diffusion. The first part dominates the temporal evolution of the parameter d , while the latter one can be extracted from the increasing width of the halo ring w , especially at long delay times, when the exciton density has already decreased by 1 to 2 orders of magnitude. The time evolution of $w^2 = 2\sigma^2$ is analyzed for delay times > 700 ps and the diffusion coefficient D can be calculated as follows:

$$D = \frac{w^2 - w_{700\text{ps}}^2}{4(t - t_{700\text{ps}})} \quad (4)$$

In the second approach, we use the low excitation power regime, where exciton diffusion is independent of the excitation density (excitation power 5 nW) and no halo formation is visible. To decrease the measurement time we measure the diffusion only in one dimension instead of the

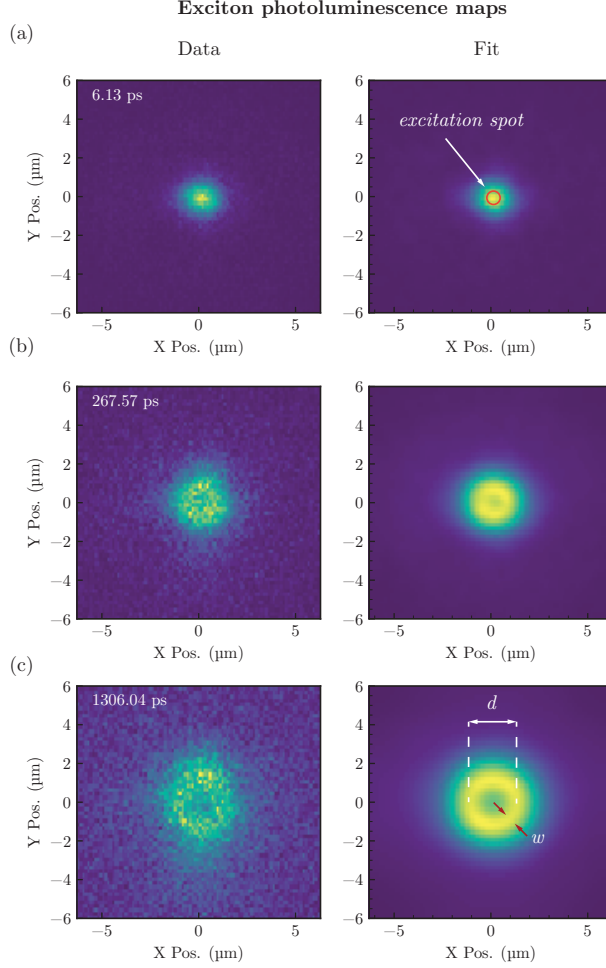


Figure 4: **Exciton photoluminescence maps for different delay times.** (a)-(c) Exemplary PL maps of a strained WS₂ monolayer for different delay times after femtosecond excitation. The left column depicts the experimental data and the right column the fit with a donut-like function. A strain direction-dependent effect on the diffusion is not observable.

entire PL image, i.e. we measure a horizontal cut through the center of the excitation spot, which has a Gaussian shape (no halo). Therefore, the experimental data can be modeled by a Gaussian function with the width w and the diffusion coefficient D can be calculated by

$$D = \frac{w^2 - w_{0\text{ps}}^2}{4t} . \quad (5)$$

Figure 5 presents the results of the two measurement approaches and compares them to the theoretical prediction. Both approaches yield the same qualitative trend and show a very good agreement with the theory.

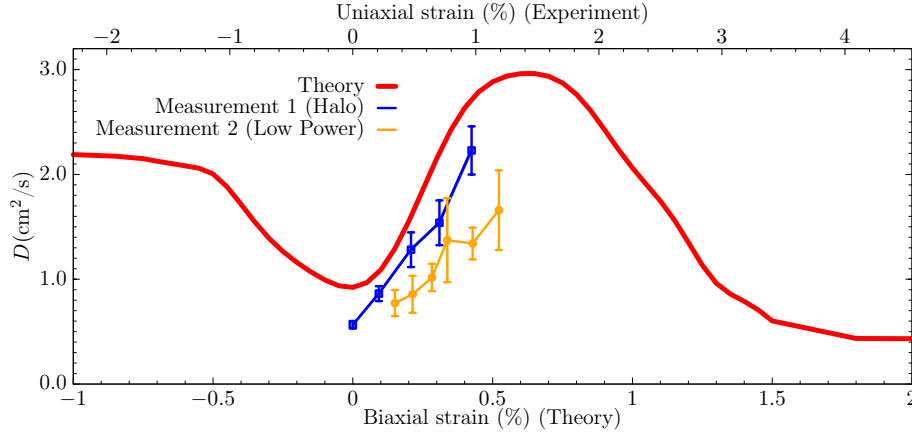


Figure 5: Comparison of the experimental diffusion coefficients (measured with the two approaches described in the text) and the theoretical prediction.

References

- [1] A. Kormányos, G. Burkard, M. Gmitra, J. Fabian, V. Zólyomi, N. D. Drummond, and V. Fal'ko. k-ptheory for two-dimensional transition metal dichalcogenide semiconductors. *2D Mater.* **2**, 022001 (2015).
- [2] Z. Khatibi, M. Feierabend, M. Selig, S. Brem, C. Linderälv, P. Erhart, and E. Malic. Impact of strain on the excitonic linewidth in transition metal dichalcogenides. *2D Mater.* **6**, 015015 (2018).
- [3] S. Brem, J. Zipfel, M. Selig, A. Raja, L. Waldecker, J. D. Ziegler, T. Taniguchi, K. Watanabe, A. Chernikov, and E. Malic. Intrinsic lifetime of higher excitonic states in tungsten diselenide monolayers. *Nanoscale* **11**, 12381 (2019).
- [4] A. Laturia, M. L. Van de Put, and W. G. Vandenberghe. Dielectric properties of hexagonal boron nitride and transition metal dichalcogenides: from monolayer to bulk. *npj 2D Materials and Applications* **2**, 6 (2018).
- [5] R. Geick, C. H. Perry, and G. Rupprecht. Normal modes in hexagonal boron nitride. *Phys. Rev.* **146**, 543 (1966).
- [6] F. Gao, Y. Gong, M. Titze, R. Almeida, P. M. Ajayan, and H. Li. Valley trion dynamics in monolayer MoSe₂. *Phys. Rev. B* **94**, 245413 (2016).
- [7] T. Kato and T. Kaneko. Transport dynamics of neutral excitons and trions in monolayer ws₂. *ACS Nano* **10**, 9687 (2016).
- [8] F. Cadiz, C. Robert, E. Courtade, M. Manca, L. Martinelli, T. Taniguchi, K. Watanabe, T. Amand, A. C. H. Rowe, D. Paget, B. Urbaszek, and X. Marie. Exciton diffusion in WSe₂ monolayers embedded in a van der waals heterostructure. *Appl. Phys. Lett.* **112(15)**, 152106 (2018).

- [9] M. Titze, B. Li, X. Zhang, P. M. Ajayan, and H. Li. Intrinsic coherence time of trions in monolayer MoSe_2 measured via two-dimensional coherent spectroscopy. *Phys. Rev. Materials* **2**, 054001 (2018).
- [10] M R Molas, C Faugeras, A O Slobodeniuk, K Nogajewski, M Bartos, D M Basko, and M Potemski. Brightening of dark excitons in monolayers of semiconducting transition metal dichalcogenides. *2D Mater.* **4**, 021003 (2017).
- [11] S. Brem, M. Selig, G. Berghäuser, and E. Malic. Exciton relaxation cascade in two-dimensional transition metal dichalcogenides. *Sci. Rep.* **8**, 8238 (2018).
- [12] Faris Kadi, Torben Winzer, Ermin Malic, Andreas Knorr, F. Göttfert, M. Mittendorff, S. Winnerl, and M. Helm. Microscopic description of intraband absorption in graphene: The occurrence of transient negative differential transmission. *Phys. Rev. Lett.* **113**, 035502 (2014).
- [13] Z. Jin, X. Li, J. T. Mullen, and K. W. Kim. Intrinsic transport properties of electrons and holes in monolayer transition-metal dichalcogenides. *Phys. Rev. B* **90**, 045422 (2014).
- [14] M. Selig, G. Berghäuser, M. Richter, R. Bratschitsch, A. Knorr, and E. Malic. Dark and bright exciton formation, thermalization, and photoluminescence in monolayer transition metal dichalcogenides. *2D Mater.* **5**, 035017 (2018).
- [15] R. Rosati, R. Perea-Causín, S. Brem, and E. Malic. Negative effective excitonic diffusion in monolayer transition metal dichalcogenides. *Nanoscale* **12**, 356 (2020).
- [16] O. B. Aslan, M. Deng, and T. F. Heinz. Strain tuning of excitons in monolayer WSe_2 . *Phys. Rev. B* **98**, 115308 (2018).
- [17] Y.P. Varshni. Temperature dependence of the energy gap in semiconductors. *Physica* **34**, 149 (1967).
- [18] K. P. O' Donnell and X. Chen. Temperature dependence of semiconductor band gaps. *Appl. Phys. Lett.* **58**, 2924 (1991).
- [19] P. Nagler, M. V. Ballottin, A. A. Mitioglu, M. V. Durnev, T. Taniguchi, K. Watanabe, A. Chernikov, C. Schüller, M. M. Glazov, P. C. M. Christianen, and T. Korn. Zeeman splitting and inverted polarization of biexciton emission in monolayer WS_2 . *Phys. Rev. Lett.* **121**, 057402 (2018).
- [20] Y. Uchiyama, A. Kutana, K. Watanabe, T. Taniguchi, K. Kojima, T. Endo, Y. Miyata, H. Shinohara, and R. Kitaura. Momentum-forbidden dark excitons in hBN-encapsulated monolayer MoS_2 , *npj 2D Mater. and Appl.* **3**, 26 (2019).
- [21] T. Deilmann and K. S. Thygesen, Finite-momentum exciton landscape in mono- and bilayer transition metal dichalcogenides, *2D Mater.* **6**, 035003 (2019).
- [22] R. Schmidt, I. Niehues, R. Schneider, M. Drüppel, T. Deilmann, M. Rohlfig, S. Michaelis de Vasconcellos, A. Castellanos-Gomez, and R. Bratschitsch. Reversible uniaxial strain tuning in atomically thin WSe_2 . *2D Mater.* **3**, 021011, (2016).

- [23] R. Schmidt, G. Berghäuser, R. Schneider, M. Selig, P. Tonndorf, E. Malic, A. Knorr, S. Michaelis de Vasconcellos, and R. Bratschitsch. Ultrafast coulomb-induced intervalley coupling in atomically thin WS₂. *Nano Lett.* **16**, 2945 (2016).
- [24] M. Kulig, J. Zipfel, P. Nagler, S. Blanter, C. Schüller, T. Korn, N. Paradiso, M. M. Glazov, and A. Chernikov. Exciton Diffusion and Halo Effects in Monolayer Semiconductors. *Phys. Rev. Lett.* **120**, 207401 (2018).